

# PNAS



## Supporting Information for

### Supplementary Materials for: Observation of the most H<sub>2</sub>-dense filled ice under high pressure

Umbertoluca Ranieri, Simone Di Cataldo, Maria Rescigno, Lorenzo Monacelli, Richard Gaal, Mario Santoro, Leon Andriambariarijaona, Paraskevas Parisiades, Cristiano De Michele, and Livia Eleonora Bove

Corresponding Author: Livia Eleonora Bove.

E-mail: [livia.bove@epfl.ch](mailto:livia.bove@epfl.ch)

#### This PDF file includes:

- Supporting text
- Figs. S1 to S15
- Tables S1 to S2
- SI References

## Supporting Information Text

### 1. Computational details

**Crystal structure prediction.** The convex hulls in Fig. S1 were obtained by combining the results from two different structural searches, plus additional calculations. The calculations performed were the following:

- One structural search using the molecular geometry constrained to H<sub>2</sub>O and H<sub>2</sub> units, a variable number of molecules of each type, and a unit cell going from a minimum of 6 to a maximum of 12 molecules. These calculation were performed using an initial population size of 80 individuals and subsequent populations of 40 individuals, for a total of 30 generations ( 1200 structures)
- One structural search using no constraints on the molecular geometry, a variable number of atoms of each type, and a unit cell going from a minimum of 24 to a maximum of 48 atoms per unit cell. These calculations were performed using an initial population of 80 individuals and a subsequent population of 40 individuals, for a total of 40 generations ( 1600 structures)
- **Only at 20 and 40 GPa:** manual addition of the following structures: C<sub>0</sub> phase, Ice VII phase with one and two interstitial H<sub>2</sub> molecules per H<sub>2</sub>O, methane hydrate-like phases, where H<sub>2</sub> is substituted to methane. In Fig. S1 these are labeled as: C<sub>0</sub>, ICE-VII+H<sub>2</sub>, ICE-VII+2H<sub>2</sub>, MH III+H<sub>2</sub>, MH III+2H<sub>2</sub>, MH IV+H<sub>2</sub>, and MH IV+2H<sub>2</sub>, respectively. These structures were relaxed using the same settings as the others, and added to the pool of structures to compute the convex hull.

Structural relaxations were performed using Density Functional Theory (DFT) as implemented in the Vienna ab-initio Simulation Package (VASP) (1), with a projector-augmented wave pseudopotentials with PBE exchange-correlation functional supplied with the package (2). In the structural relaxations, a five-step approach was employed, using progressively tighter constraints on the structural relaxation.

**Zero-point energy.** In hydrogen-rich materials, phonons are highly energetic, hence the vibrational zero-point energy can change the total energy of a structure significantly (zero-point energy or ZPE). To maintain the computational costs manageable, we performed the structural searches without including the ZPE, and then added it as a correction only to the C<sub>2</sub> and C<sub>3</sub> phases, and to the endpoints of the convex hull.

The ZPE was evaluated using Density Functional Perturbation Theory by computing the harmonic dynamical matrices on a 2×2×2 grid, and then using Fourier interpolation on a 16×16×16 to compute the phonon DOS. The ZPE is then calculated as:

$$E_{ZP} = \int_0^{\omega_{max}} \frac{\hbar\omega}{2} F(\omega) d\omega \quad [1]$$

where  $F(\omega)$  is the phonon Density of States. A post-processing python script was employed to performed the integral using the trapezoidal rule.

**Effect of the exchange-correlation functional on the total energy.** To evaluate the impact of the different functionals onto the total energy, we compared the enthalpy of the C<sub>2</sub> and C<sub>3</sub> phases at 10, 20, and 40 GPa using three different functionals: PBE, optB88, and B3LYP. As shown in Fig. S2, the difference between functionals does not depend significantly on pressure, but is rather significant especially in the C<sub>2</sub> phase, where it amounts to about 20 meV/H<sub>2</sub>O.

### 2. Phonon calculations

Phonon calculations and Raman intensities within the harmonic approximation were performed using Quantum ESPRESSO (3, 4), employing Optimized Norm-Conserving Vanderbilt pseudopotentials (ONCV) (5). A cutoff of 90 Ry was employed on the plane waves expansion. A 4×4×4 grid in reciprocal space with fixed occupations was employed.

**A. Frequency corrections to the harmonic Raman spectrum.** An accurate determination of the frequency of vibration of the H<sub>2</sub> molecule requires taking into account both anharmonic effects and the quantum nature of the proton. These effects are both beyond the harmonic approximation but can be described within the Stochastic Self-Consistent Harmonic Approximation (SSCHA) (6, 7). In addition, even the choice of the exchange-correlation functional is known to be crucial (8), and the Becke-Lee-Yang-Parr (BLYP) is commonly accepted to be the most accurate.

To keep the computational costs manageable, we computed an effective correction to the harmonic frequencies, which was then used to shift the harmonic result calculated with the optB88 functional at all pressures.

The correction was computed as the sum of two terms, averaged over the whole pressure range:

- $\Delta\omega_{SSCHA, opt88} = \omega_{SSCHA, optB88} - \omega_{H, optB88}$  where  $\omega_{SSCHA, optB88}$  and  $\omega_{H, optB88}$  are the frequencies of the mode with the strongest Raman intensity (after scaling it with its calculated depolarization ratio) calculated within the SSCHA and within the harmonic approximation, respectively, both with optB88 exchange-correlation functional.

- $\Delta\omega_{H,BLYP} = \omega_{H,BLYP} - \omega_{H,optB88}$ , where  $\omega_{H,BLYP}$  and  $\omega_{H,optB88}$  are the frequencies of the mode with the strongest Raman intensity calculated within the harmonic approximation using a BLYP and optB88 exchange-correlation functional, respectively.

Then, the corrected frequencies  $\tilde{\omega}$  were computed as:

$$\tilde{\omega} = \omega_{H,optB88} + \Delta\omega_{SSCHA,optB88} + \Delta\omega_{H,BLYP}. \quad [2]$$

Tab. S1 reports the used values. Standard DFT customarily overestimates H<sub>2</sub> vibron frequencies and here we remarkably obtain a very good agreement with the experimental frequencies when both corrections due to the exchange-correlation functional, and anharmonic and quantum effects are taken into account (see Fig. 3 of the main text). For reference, in Fig. S3 we report the analogous of Fig. 3 of the main text without including any correction.

	C <sub>2</sub>	C <sub>3</sub>
$\Delta\omega_{SSCHA,optB88} (cm^{-1})$	-266	-313
$\Delta\omega_{H,BLYP} (cm^{-1})$	82	79
$\Delta\omega_{SSCHA,optB88} + \Delta\omega_{H,BLYP} (cm^{-1})$	-184	-234

**Table S1. Summary of the calculated frequency shifts for the C<sub>2</sub> and C<sub>3</sub> phases.**

**B. SSCHA calculations.** The SSCHA calculation was performed on a 2x2x1 supercell for both the C<sub>2</sub> and C<sub>3</sub> phases, containing 80 and 112 atoms, respectively. Due to the local nature of the H<sub>2</sub> vibration, the supercell considered is sufficient to converge the Raman spectrum. The SSCHA calculation was performed at 5, 10, 20, 30, 40, 60, and 80 GPa pressures for the C<sub>2</sub>, and 30, 40, 60, and 80 GPa for the C<sub>3</sub>; all simulations were performed at 0 K. At each pressure, the primitive cell was relaxed, accounting for quantum fluctuations using the method described in ref. (7). The free energy optimization within the SSCHA was performed starting with small populations of 800 configurations for 25-30 iterations, with a last shot of 20000 or 40000 configurations to properly converge the stochastic noise and get accurate values of the anharmonic shift of the Raman active H<sub>2</sub> vibron. The frequency shift was compared with the peak position of the full Raman spectrum, evaluated within the time-dependent self-consistent harmonic approximation (TD-SCHA) as illustrated in refs. (9, 10), obtaining compatible values.

As an energy/force calculator for the SSCHA, we employed DFT with the optB88 exchange-correlation functional as described above, with the k-mesh sampling appropriately rescaled to take into account the supercell.

### 3. Thermodynamical stability

The thermodynamically stable phases at various pressures were determined using evolutionary algorithms for crystal structure prediction, as implemented in the USPEX code (11, 12). In Fig. S4, we show the formation enthalpy of the C<sub>2</sub> and C<sub>3</sub> phases as a function of pressure, including both zero point effect and an estimate of the error due to the choice of the exchange-correlation functional. On qualitative ground, the origin of the high-pressure instability for the C<sub>2</sub> phase can be found in Fig. S5. As shown, the C<sub>2</sub> phase occupies a slightly larger volume than water and hydrogen, which makes it energetically unfavorable at high pressure. The C<sub>3</sub> phase, on the other hand, occupies slightly less volume than its constituents, hence it remains stable even at the extreme pressure of 200 GPa.

### 4. Additional structural information

In this section, we provide complementary information on the computationally optimized crystal structures of the C<sub>2</sub> and C<sub>3</sub> phases. Structural details for the C<sub>2</sub> phase at 10 and 40 GPa, and for the C<sub>3</sub> phase at 40 GPa are reported in Tab. S2. The simulated (proton-ordered) C<sub>2</sub> phase can be described by the orthorhombic space group  $Pna2_1$  (n. 33) at both pressures and the simulated (proton-ordered) C<sub>3</sub> phase can be described by the tetragonal space group  $P4_1$  (n. 76). One can easily check that C<sub>2</sub> at 10 GPa and C<sub>3</sub> at 40 GPa correspond to the  $Fd\bar{3}m$  structures given in the main text, after removing the H atoms of the water molecules and substituting the H<sub>2</sub> molecules by a single atom sitting in the center of mass. The simulated C<sub>2</sub> phase at 40 GPa is a significant distortion of the same structure, with the hexagons formed by the water molecules being elongated along the  $c$  axis. As shown below in this section, the distortion is progressive. By transitioning from C<sub>2</sub> to C<sub>3</sub>, the system entirely recovers its initial water sublattice ( $Fd\bar{3}m$  is also the space group of ice Ic).

The simulated unit cell dimensions of the C<sub>2</sub> and C<sub>3</sub> phases as a function of pressure are reported in Fig. S8, where we multiplied the  $a$  and  $b$  lattice parameters by  $\sqrt{2}$  to match them with the lattice parameter of the corresponding cubic structure (the unit cell of the  $Fd\bar{3}m$  structure is twice as big in volume and obviously contains twice as many H<sub>2</sub>O and H<sub>2</sub> molecules). Figure S9 reports the calculated H<sub>2</sub>-H<sub>2</sub>, O-O, and O-H<sub>2</sub> distances as a function of pressure. This involved using the coordinate of the center of mass of each H<sub>2</sub> molecule. We note that in the C<sub>2</sub> phase, a significant change in the second nearest-neighbor shell occurs starting from 20 GPa (see Fig. S9). This happens concomitantly with an alignment of the H<sub>2</sub> molecules along the  $c$  axis of the structure. The angle formed between the H<sub>2</sub> molecule and the  $c$  axis in the C<sub>2</sub> phase is reported in Fig. S8. The angle indeed starts to progressively change upon compression above 20 GPa. At 50 GPa, the H<sub>2</sub> molecules are perfectly aligned along the  $c$  axis and the O-H bond symmetrizes, leading to an increase in symmetry from the  $Pna2_1$  to the  $I4_1amd$  (n. 141) space group.

On the other hand, in the  $C_3$  phase, no such a distortion of the water sublattice is found in our simulations and no collective alignment of the  $H_2$  molecules of any kind is observed. Also, we note that at the DFT level in the  $C_3$  phase, the O-H symmetrization only occurs above 120 GPa and is not associated with a change in the space group. Finally, we point out that the distortion emerging in our simulations of the  $C_2$  phase above 20 GPa cannot be confirmed nor ruled out by our experimental XRD data, as higher data quality at high angles would be required.

In Fig. S6, we show the crystal structures of the  $C_2$  and  $C_3$  phases with the charge density difference defined as follows:

$$\delta\rho(\vec{r}) = \rho_{full}(\vec{r}) - \rho_{H_2O}(\vec{r}) - \rho_{H_2}(\vec{r}), \quad [3]$$

where  $\rho_{full}$  is the ground-state charge density for the regular crystal structure, and  $\rho_{H_2O}$  and  $\rho_{H_2}$  are the ground-state charge densities for the same structure where only water and hydrogen are present, respectively. In other words,  $\delta\rho(\vec{r})$  shows how the charge density changes between the complete structure and its constituents. The distribution  $\delta\rho(\vec{r})$  between the  $C_2$  and  $C_3$  structures are quite similar, with only a few subtle differences. In particular, in the  $C_2$  phase, the negative charge is quite homogeneous around each  $H_2$  molecule, and distributes in a dome-like shape around oxygen on the side opposite to the two hydrogen atoms of the  $H_2O$  molecule. In  $C_3$ , on the other hand, the charge around each  $H_2$  is slightly skewed, while around oxygen is concentrated along two opposite directions, roughly towards the O-H bond.





Phase	Composition	Space Group	Pressure (GPa)	Lattice parameters (Å)	Atom	Wyckoff pos.	Coordinates
C <sub>2</sub>	H <sub>2</sub> O+H <sub>2</sub>	Pna2 <sub>1</sub> (n. 33)	10	$a = 4.166, b = 6.00, c = 4.195$ $\alpha = \beta = \gamma = 90^\circ$	O1	4a	0.00320 0.12433 0.49880
					H1	4a	0.00268 0.02962 0.69876
					H2	4a	0.03549 0.41887 0.97597
					H3	4a	0.06570 0.67251 0.53709
					H4	4a	0.19992 0.22378 0.50694
C <sub>2</sub>	H <sub>2</sub> O+H <sub>2</sub>	Pna2 <sub>1</sub> (n. 33)	40	$a = 3.581, b = 6.046, c = 3.594$ $\alpha = \beta = \gamma = 90^\circ$	O1	4a	0.00376 0.87532 0.99529
					H1	4a	0.00029 0.98731 0.22588
					H2	4a	0.00993 0.43363 0.99079
					H3	4a	0.02012 0.68492 0.50457
					H4	4a	0.22615 0.23751 0.50099
C <sub>3</sub>	H <sub>2</sub> O+2H <sub>2</sub>	P4 <sub>1</sub> (n. 76)	40	$a = b = 4.110, c = 5.843$ $\alpha = \beta = \gamma = 90^\circ$	O1	4a	-0.24923 -0.25255 -0.24965
					H1	4a	0.02528 0.31301 -0.16785
					H2	4a	-0.42917 -0.20811 0.37173
					H3	4a	-0.01611 0.19129 -0.08321
					H4	4a	0.41775 -0.29338 0.37779
					H5	4a	-0.04590 0.25474 0.40560
H6	4a	-0.45651 -0.25486 -0.15442					

**Table S2. Structural information for the C<sub>2</sub> phase at 10 and 40 GPa and for the C<sub>3</sub> phase at 40 GPa, both in their proton-ordered configurations used in our DFT calculations.**

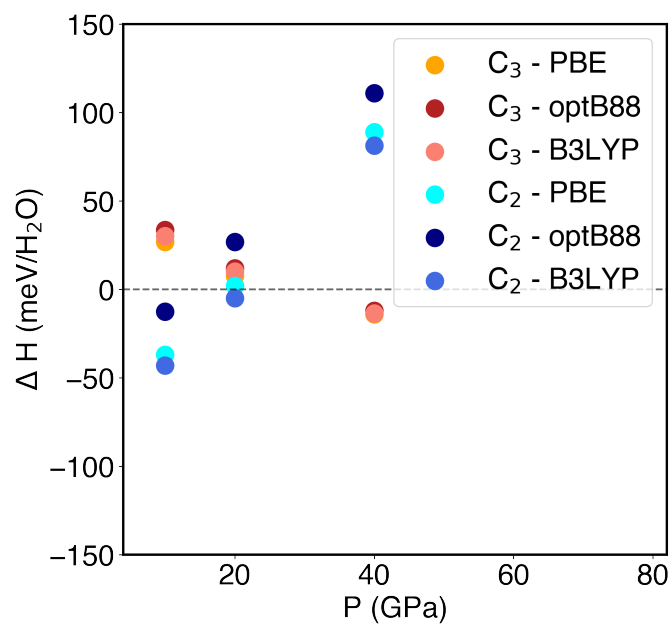


**Fig. S2.** Formation enthalpy for the C<sub>2</sub> and C<sub>3</sub> phases at 10, 20 and 40 GPa using three different exchange correlation functionals: PBE, optB88, and B3LYP.

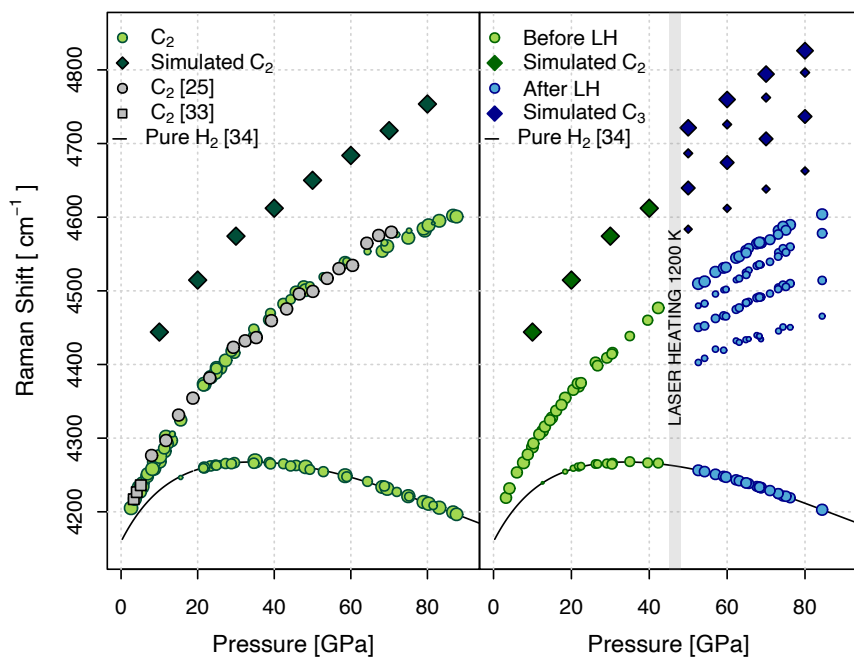


**Fig. S3.** Comparison between experimental frequencies and calculated harmonic frequencies without any correction. The experimental data is identical to Fig. 3 of the main text. The computed frequencies are obtained from Density Functional Perturbation Theory, with the optB88 exchange-correlation functional.

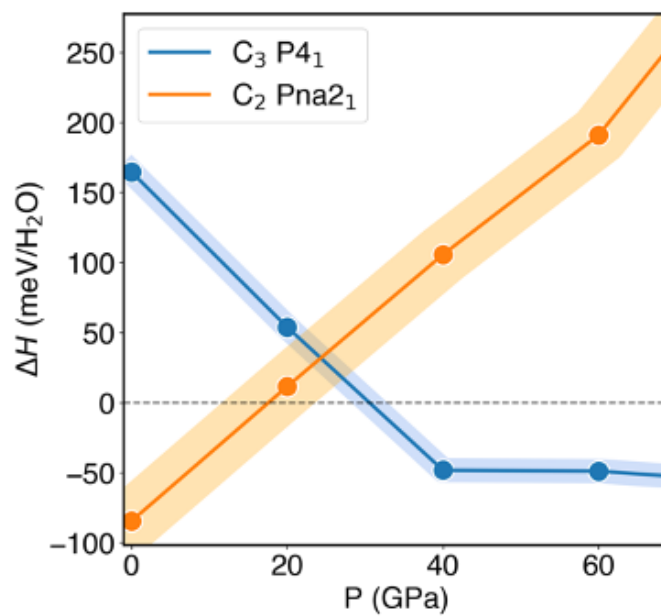


**Fig. S4.** Formation enthalpy per water molecule as a function of pressure for the C<sub>2</sub> and C<sub>3</sub> phases in their proton-ordered configuration, including  $E_{ZP}$ . The energy uncertainty due to the choice of the exchange-correlation functional (see text) is shown as a broad line.

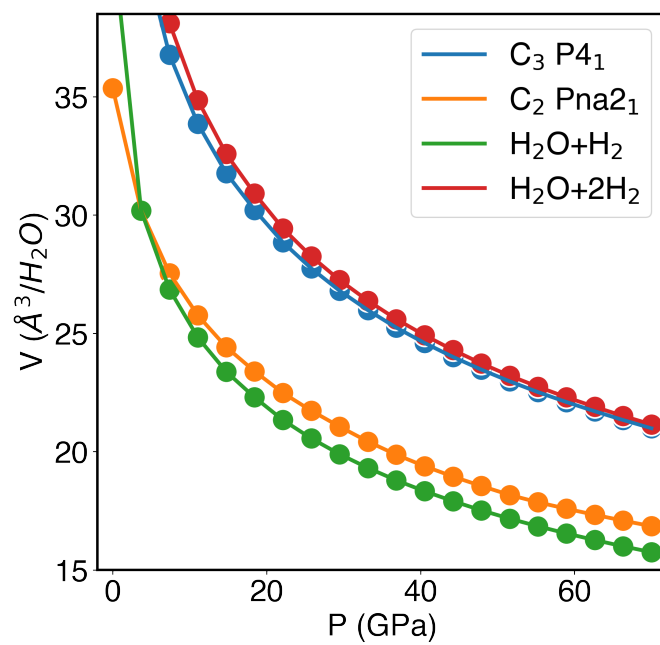


**Fig. S5.** Computational volumes per  $\text{H}_2\text{O}$  molecule for the  $\text{C}_2$  and  $\text{C}_3$  phases as a function of pressure, and computational volumes of the equivalent amounts of  $\text{H}_2$  and  $\text{H}_2\text{O}$  molecules existing in their pure separated phases.

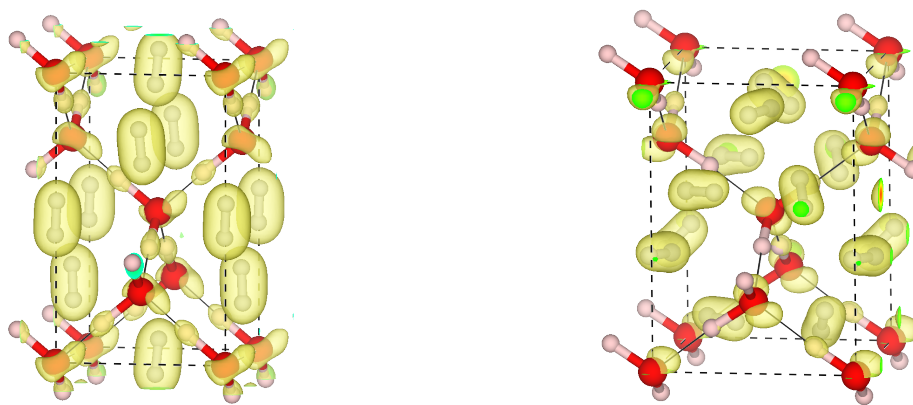


**Fig. S6.** Crystal structure with charge density difference displayed as a yellow isosurface for the  $C_2$  (left side) and  $C_3$  (right side) phases at 40 GPa. The isosurface corresponds to 10% of the maximum (positive) value of  $\delta\rho$ , as defined in the text.

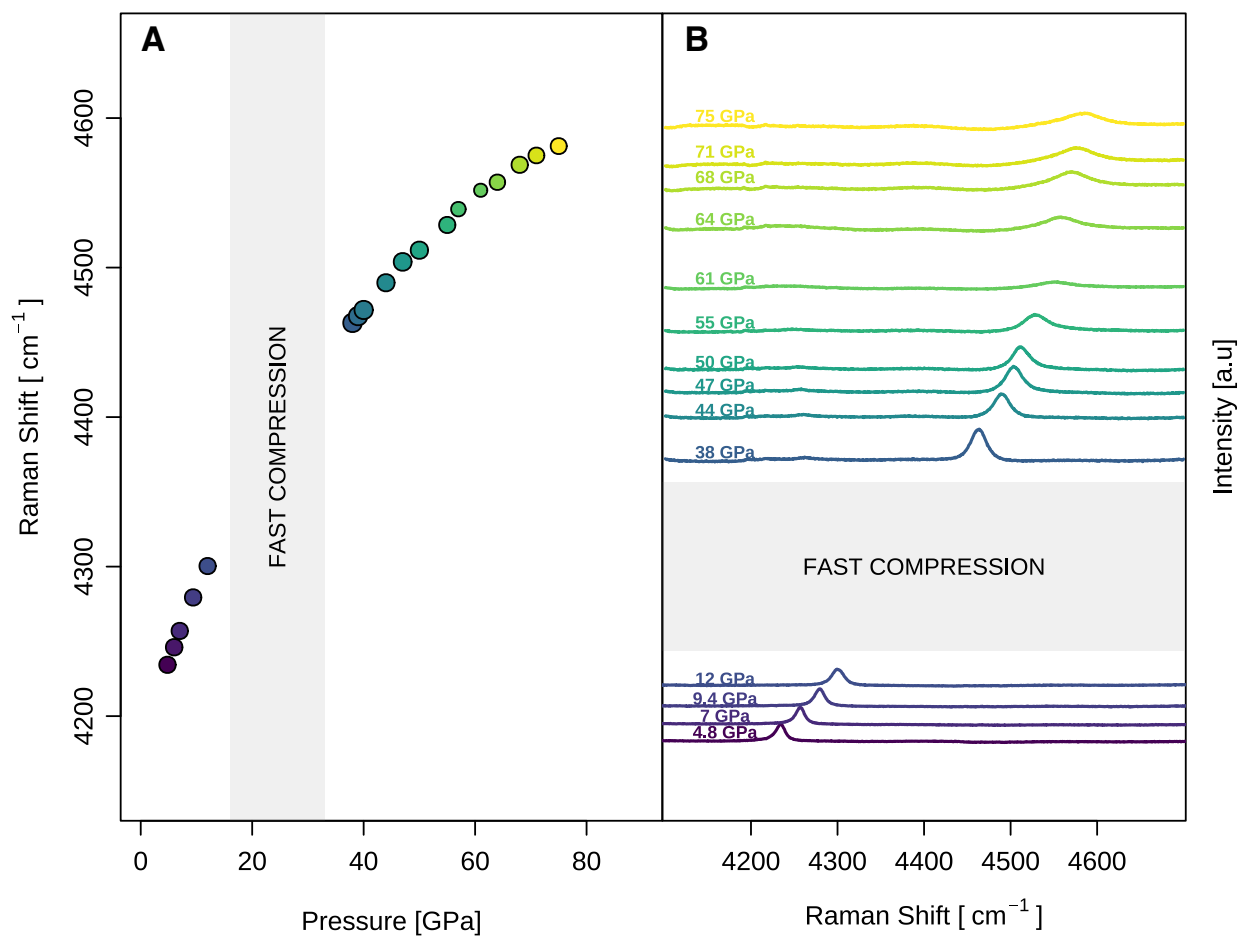


**Fig. S7.** Experimental Raman spectra (panel B) and corresponding frequencies (panel A) collected on the same sample loading. Fast compression from 14 GPa to 30 GPa allows avoiding the destabilization of the hydrate and the formation of pure  $\text{H}_2$



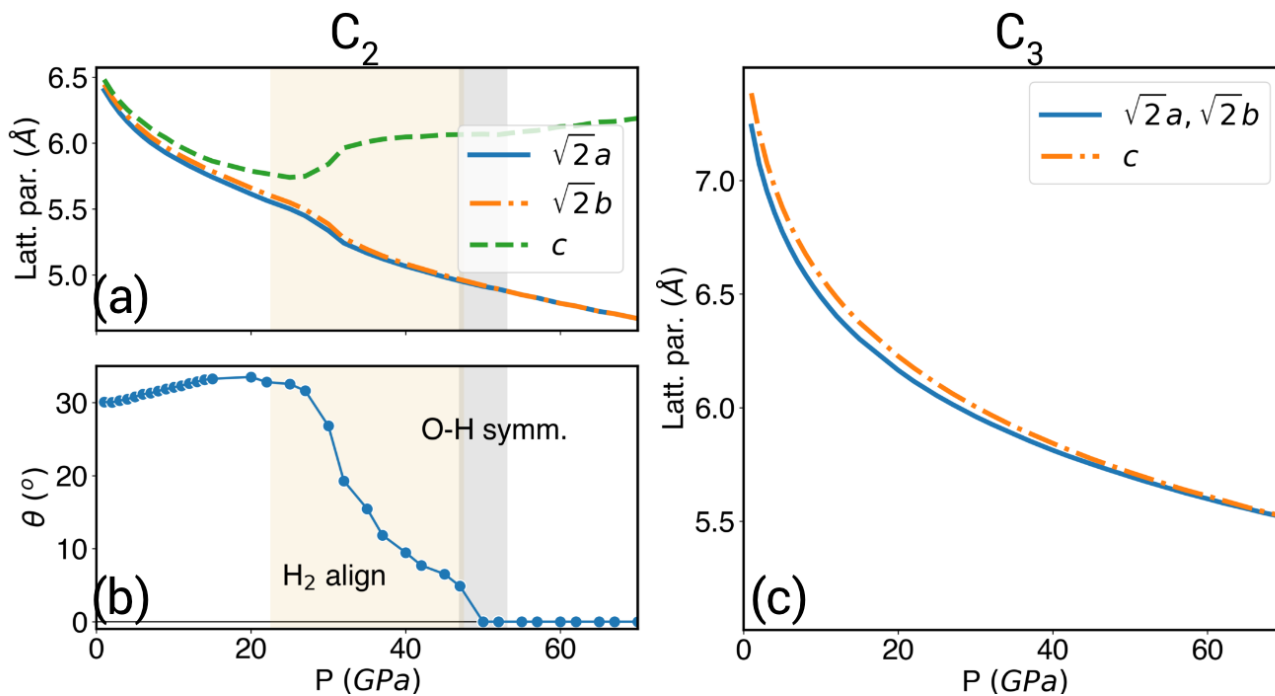


**Fig. S8.** Structural data for the simulated  $C_2$  and  $C_3$  phases as a function of pressure. Panel (a): lattice constants for the  $C_2$  phase.  $a$  and  $b$  were multiplied by  $\sqrt{2}$ . (b) angle between the  $H_2$  molecules and the  $c$  axis. The orange and gray shades highlight the regions of  $H_2$  alignment and O–H bond symmetrization, respectively. (c) lattice constants for the  $C_3$  phase.  $a$  and  $b$  were multiplied by  $\sqrt{2}$ .

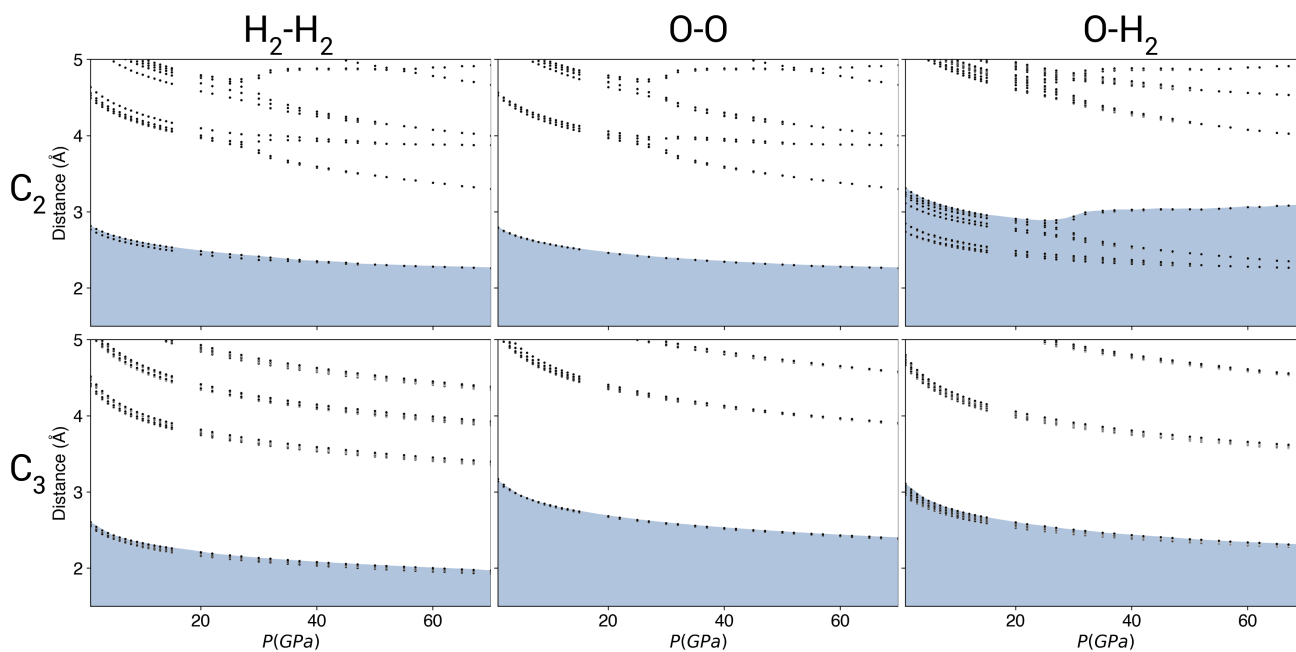


**Fig. S9.** Distances between atoms/molecules in the simulated  $C_2$  and  $C_3$  phases as a function of pressure. The distances are shown as black dots, while the first shell of nearest neighbor is highlighted as a blue shade.

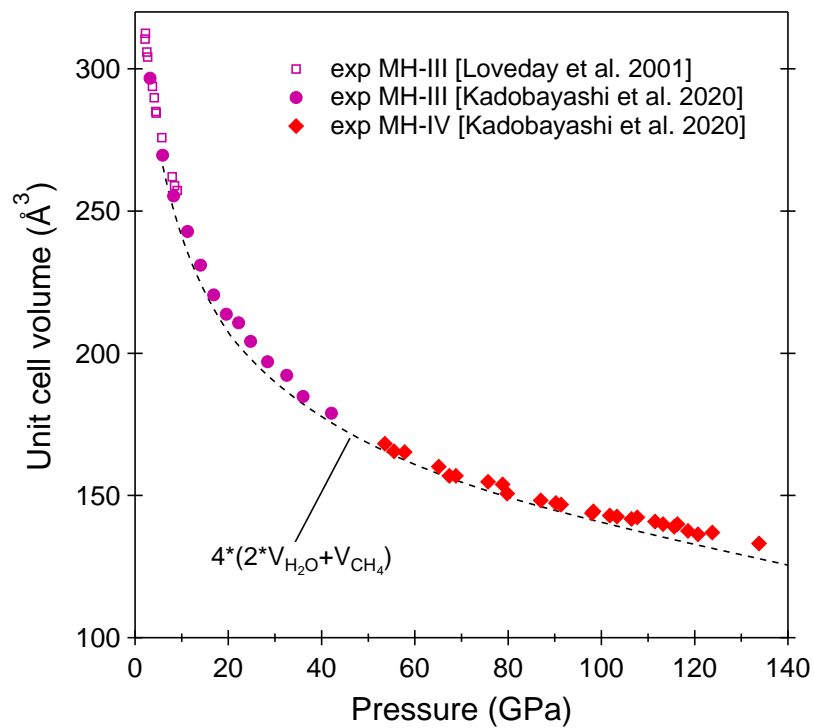


**Fig. S10.** Experimental unit cell volumes as a function of pressure for the MH-III and MH-IV phases of methane hydrate from the literature (13, 14). The dotted line represents the volume of the ideal mixture of the equivalent amount of H<sub>2</sub>O and CH<sub>4</sub> molecules, calculated using the literature equations of state (15, 16).

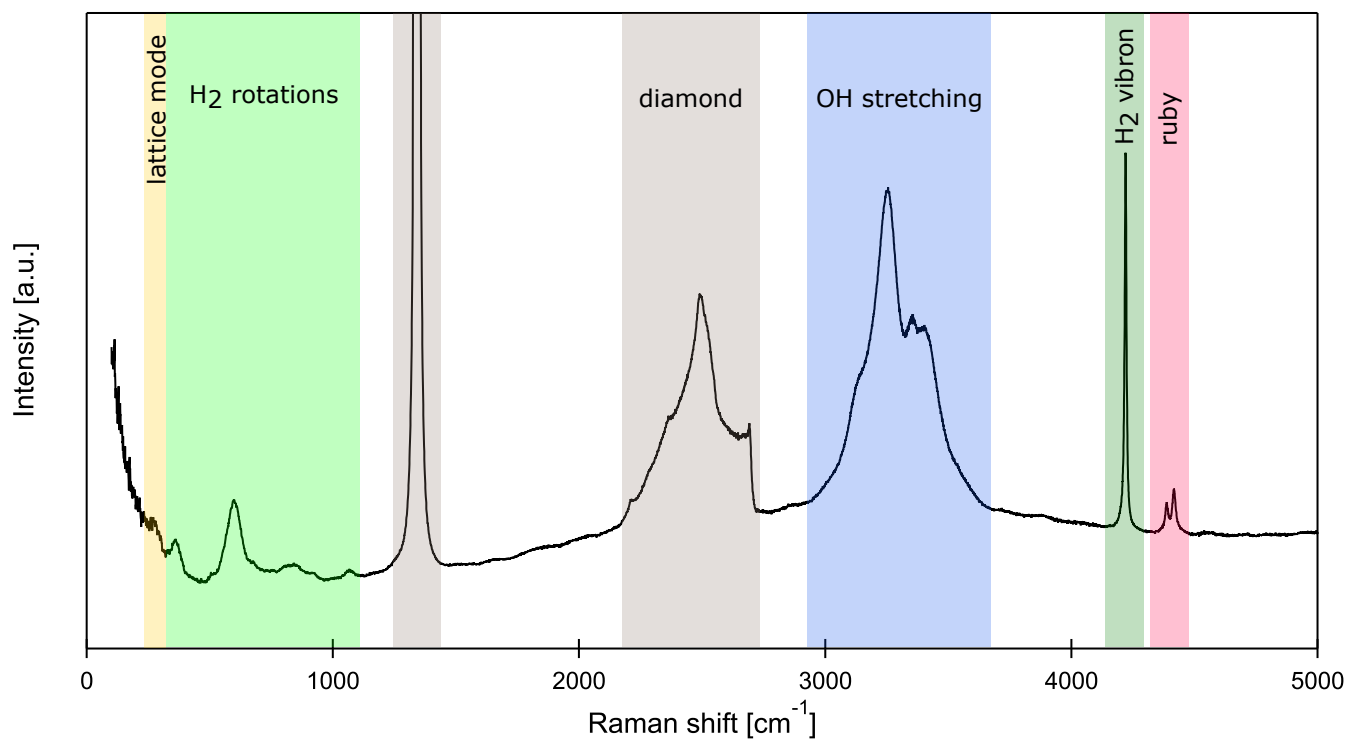


**Fig. S11.** Example of Raman spectrum of the sample (C<sub>2</sub> hydrogen hydrate and excess water ice) at 4 GPa, covering the full measured frequency range. The visible modes were assigned as reported in the figure. "Diamond" refers to the diamond anvils of the high-pressure cell; "ruby" was the pressure gauge in this sample

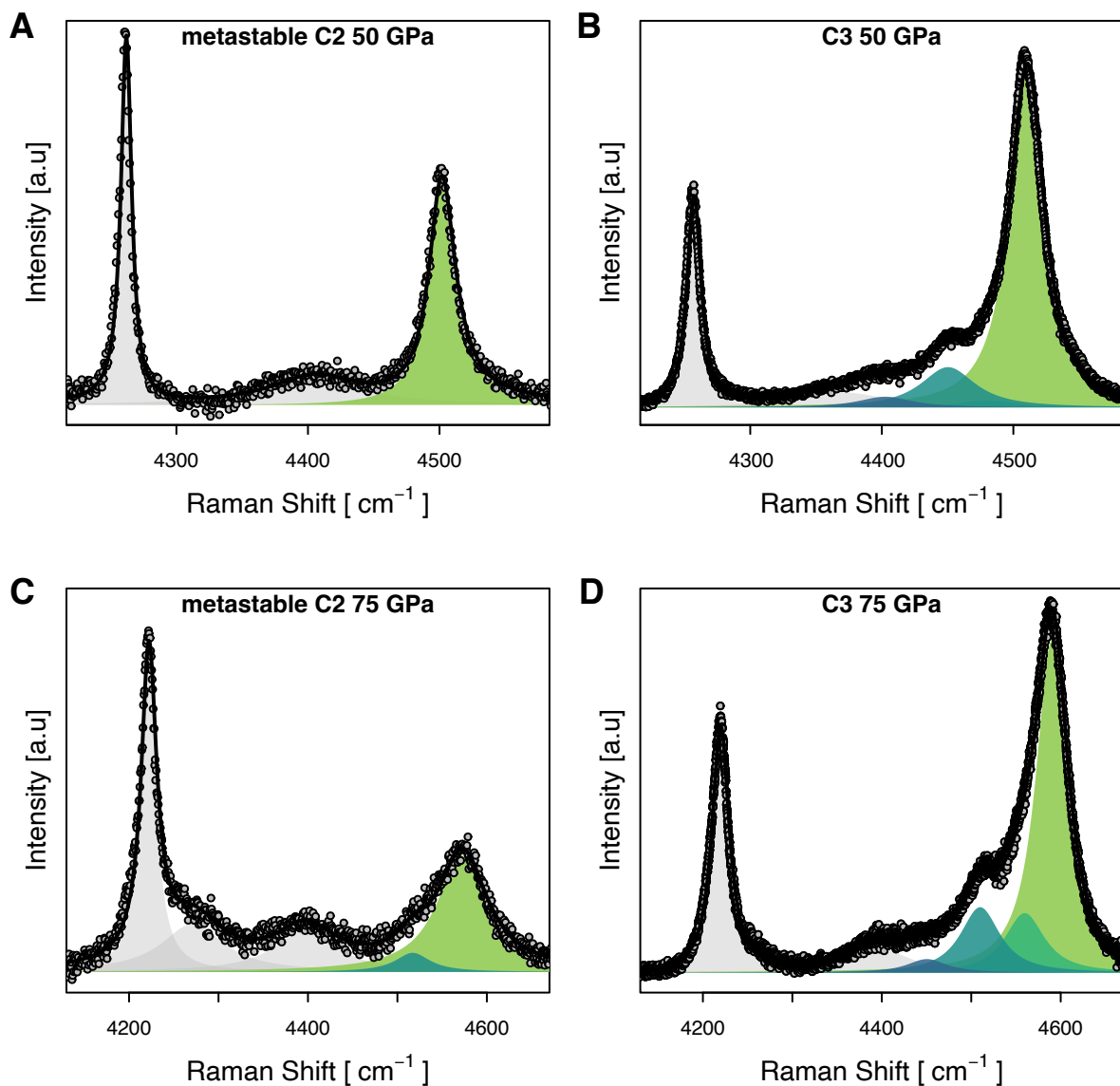


**Fig. S12.** Examples of fits to the measured Raman spectra in the  $C_2$  (panels A and C) and  $C_3$  (panels B and D) phase at around 50 and 75 GPa. Spectra were fitted using a Levenberg-Marquardt minimization algorithm over the range  $4150\text{-}4650\text{ cm}^{-1}$ . The fitting function is a Pearson VII line shape:  $y = I \left\{ \frac{1+(x-x_0)^2}{\left[2w/(1+e^{a(x-x_0)/w})\right]^{2m}} \right\}^{-m}$ , where  $m$  can be chosen to suit a particular peak shape and  $w$  is related to the peak width. An additional asymmetry parameter is used for the pure  $H_2$  and the high frequency  $C_2$  and  $C_3$  peaks. The peak position  $x_0$ , intensity  $I$ , and width  $w$  are left as free parameters. The asymmetry parameter and  $m$  are obtained through a simultaneous fit to all data. A quadratic background had been previously subtracted. The colored peaks represent peaks related to the sample while the gray shaded peaks are the pure  $H_2$  vibron peak (lower frequency) and a broad non-dispersive contribution possibly coming from partially amorphised sample.

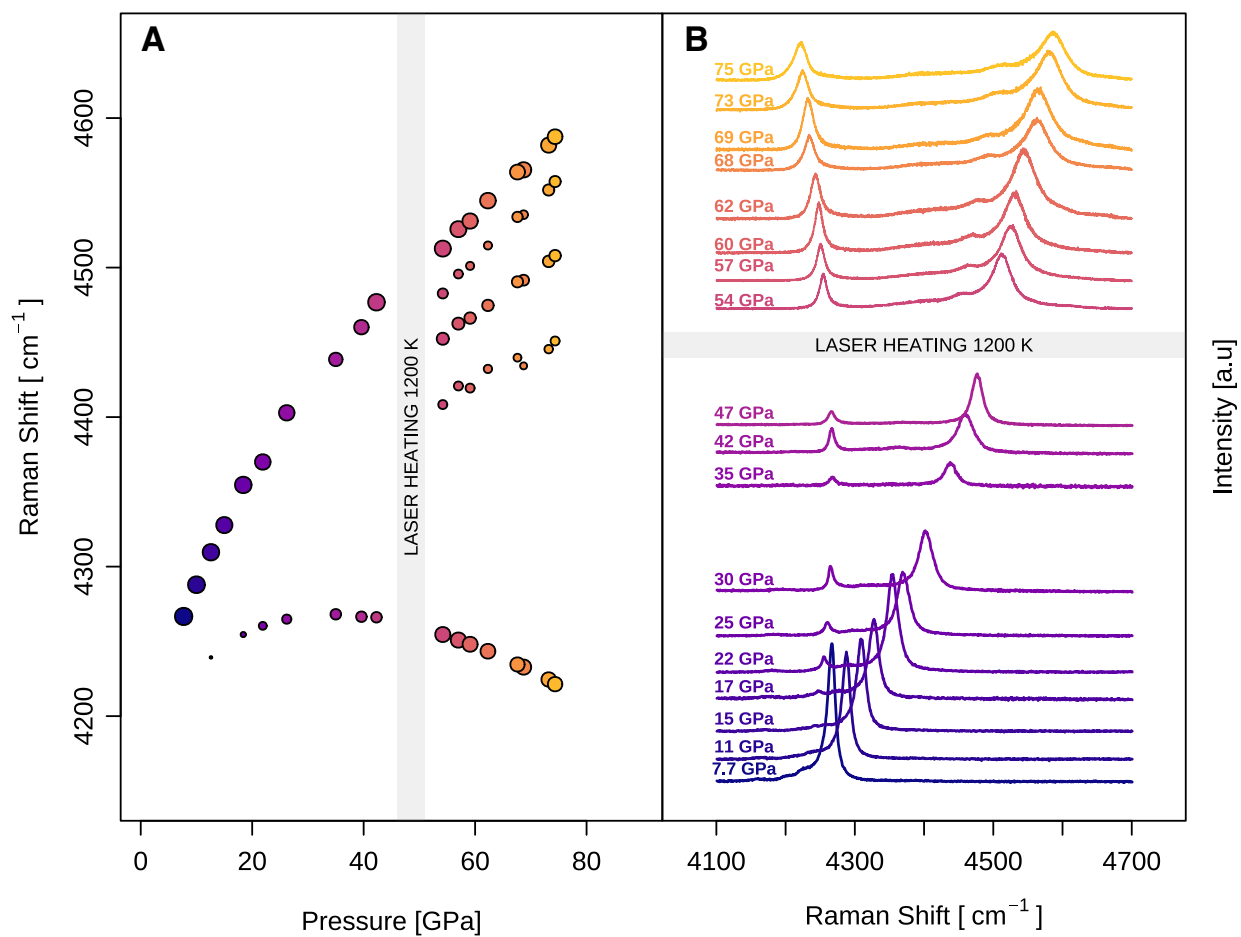


**Fig. S13.** Experimental Raman spectra (panel B) and corresponding frequencies (panel A) collected on the same sample loading before and after laser heating. The size of the dots is proportional to the peak intensity.

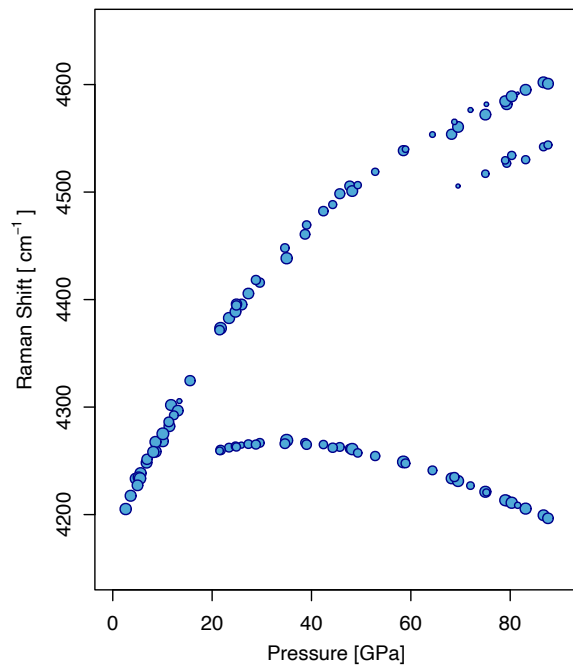


**Fig. S14.** Pressure dependence of the measured peak frequencies for the H<sub>2</sub> vibron on a sample which was not laser heated. We show the appearance of a peak at lower frequency possibly related to the formation of C<sub>3</sub> at pressures higher than 70 GPa.

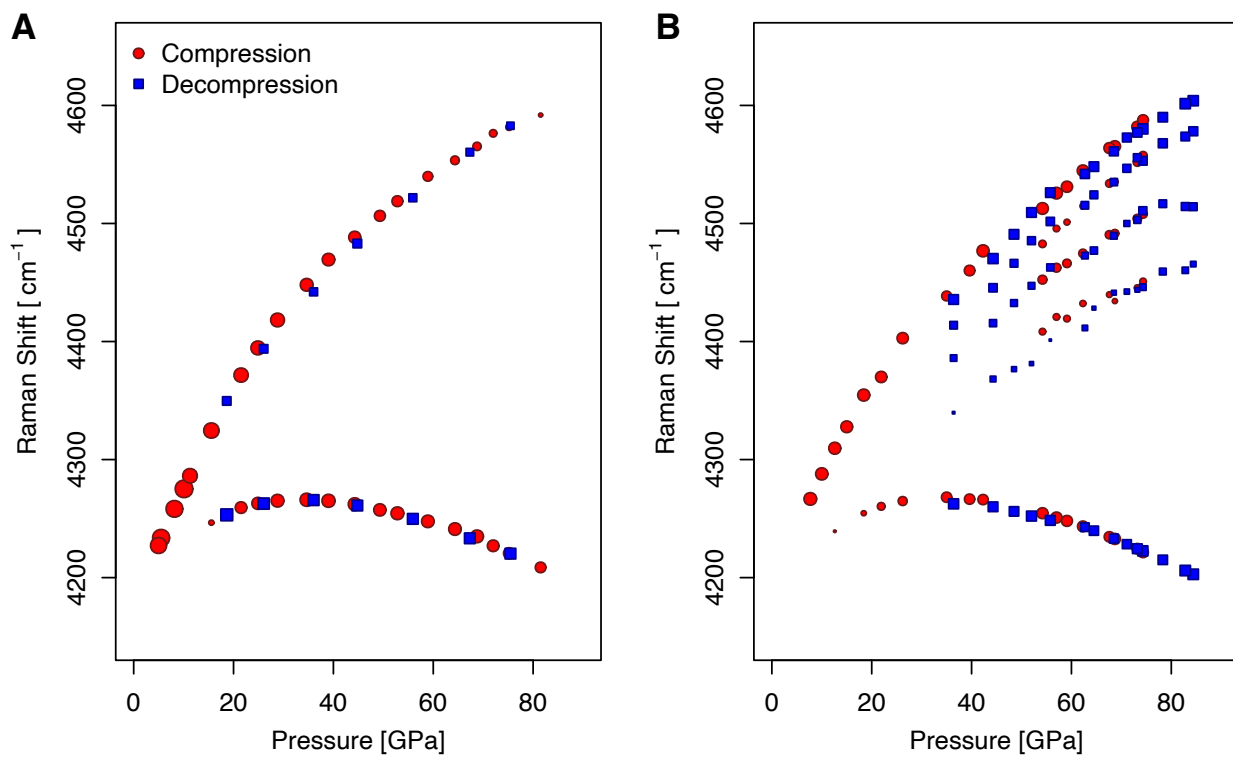


**Fig. S15.** Panel A: Experimental frequencies of the  $\text{H}_2$  vibron in the  $\text{C}_2$  phase measured on the same sample loading upon compression and decompression, as a function of pressure. Panel B: Experimental frequencies of the  $\text{H}_2$  vibron in a sample loading where Laser Heating was performed, upon compression and decompression, as a function of pressure. The size of the dots is proportional to the peak intensity.



## References

1. G Kresse, J Furthmüller, Efficient iterative schemes for *ab initio* total-energy calculations using a plane-wave basis set. *Phys. Rev. B* **54**, 11169–11186 (1996).
2. G Kresse, D Joubert, From ultrasoft pseudopotentials to the projector augmented-wave method. *Phys. Rev. B* **59**, 1758–1775 (1999).
3. P Giannozzi, et al., QUANTUM ESPRESSO: a modular and open-source software project for quantum simulation of materials. *J. Phys.: Condens. Matter* **21**, 395502 (2009).
4. P Giannozzi, et al., Advanced capabilities for materials modelling with quantum espresso. *J. Phys.: Condens. Matter* **29**, 465901 (2017).
5. DR Hamann, Optimized norm-conserving vanderbilt pseudopotentials. *Phys. Rev. B* **88**, 085117 (2017).
6. L Monacelli, et al., The stochastic self-consistent harmonic approximation: calculating vibrational properties of materials with full quantum and anharmonic effects. *J. Phys.: Condens. Matter* **33**, 363001 (2021).
7. L Monacelli, I Errea, M Calandra, F Mauri, Pressure and stress tensor of complex anharmonic crystals within the stochastic self-consistent harmonic approximation. *Phys. Rev. B* **98**, 024106 (2018).
8. RC Clay, et al., Benchmarking exchange-correlation functionals for hydrogen at high pressures using quantum monte carlo. *Phys. Rev. B* **89**, 184106 (2014).
9. L Monacelli, F Mauri, Time-dependent self-consistent harmonic approximation: Anharmonic nuclear quantum dynamics and time correlation functions. *Phys. Rev. B* **103**, 104305 (2021).
10. A Siciliano, L Monacelli, G Caldarelli, F Mauri, Wigner gaussian dynamics: Simulating the anharmonic and quantum ionic motion. *Phys. Rev. B* **107**, 174307 (2023).
11. CW Glass, AR Oganov, N Hansen, USPEX–evolutionary crystal structure prediction. *Comput. Phys. Commun.* **175**, 713–720 (2006).
12. AO Lyakhov, AR Oganov, HT Stokes, Q Zhu, New developments in evolutionary structure prediction algorithm USPEX. *Comput. Phys. Commun.* **184**, 1172–1182 (2013).
13. JS Loveday, RJ Nelmes, M Guthrie, DD Klug, JS Tse, Transition from cage clathrate to filled ice: The structure of methane hydrate III. *Phys. Rev. Lett.* **87**, 215501 (2001).
14. H Kadobayashi, et al., Structural evolution of methane hydrate under pressures up to 134 GPa. *J. Chem. Phys.* **152**, 194308 (2020).
15. S Klotz, et al., Bulk moduli and equations of state of ice VII and ice VIII. *Phys. Rev. B* **95**, 174111 (2017).
16. L Sun, et al., X-ray diffraction studies and equation of state of methane at 202 GPa. *Chem. Phys. Lett.* **473**, 72–74 (2009).